



HAL
open science

Relations between phenomenological and physical parameters in the hot coronae of AGNs computed with the MoCA code

R. Middei, S. Bianchi, A. Marinucci, G. Matt, Pierre-Olivier Petrucci, F. Tamborra, A. Tortosa

► To cite this version:

R. Middei, S. Bianchi, A. Marinucci, G. Matt, Pierre-Olivier Petrucci, et al.. Relations between phenomenological and physical parameters in the hot coronae of AGNs computed with the MoCA code. *Astronomy & Astrophysics - A&A*, 2019, 630, pp.A131. 10.1051/0004-6361/201935881 . hal-03014147

HAL Id: hal-03014147

<https://hal.science/hal-03014147v1>

Submitted on 20 Nov 2020

HAL is a multi-disciplinary open access archive for the deposit and dissemination of scientific research documents, whether they are published or not. The documents may come from teaching and research institutions in France or abroad, or from public or private research centers.

L'archive ouverte pluridisciplinaire **HAL**, est destinée au dépôt et à la diffusion de documents scientifiques de niveau recherche, publiés ou non, émanant des établissements d'enseignement et de recherche français ou étrangers, des laboratoires publics ou privés.

Relations between phenomenological and physical parameters in the hot coronae of AGNs computed with the MoCA code

R. Middei¹, S. Bianchi¹, A. Marinucci^{1,2}, G. Matt¹, P.-O. Petrucci³, F. Tamborra⁴, and A. Tortosa⁵

¹ Dipartimento di Matematica e Fisica, Università degli Studi Roma Tre, Via della Vasca Navale 84, 00146 Roma, Italy
e-mail: riccardo.middei@uniroma3.it

² ASI – Unità di Ricerca Scientifica, Via del Politecnico snc, 00133 Roma, Italy

³ Univ. Grenoble Alpes, CNRS, IPAG, 38000 Grenoble, France

⁴ Nicolaus Copernicus Astronomical Center of the Polish Academy of Sciences, ul. Bartycka 18, 00716 Warsaw, Poland

⁵ INAF/Istituto di Astrofisica e Planetologia Spaziali, Via Fosso del Cavaliere, 00133 Roma, Italy

Received 13 May 2019 / Accepted 8 August 2019

ABSTRACT

Context. The primary X-ray emission in active galactic nuclei (AGNs) is widely believed to be due to Comptonisation of the thermal radiation from the accretion disc in a corona of hot electrons. The resulting spectra can, in first approximation, be modelled with a cut-off power law, the photon index and the high-energy roll-over encoding information on the physical properties of the X-ray emitting region. The photon index and the high-energy curvature of AGNs (Γ , E_c) have been largely studied since the launch of X-ray satellites operating above 10 keV. However, high-precision measurements of these two observables have only been obtained in recent years thanks to the unprecedented sensitivity of *NuSTAR* up to 79 keV.

Aims. We aim at deriving relations between Γ , E_c phenomenological parameters and the intrinsic properties of the X-ray-emitting region (the hot corona), namely the optical depth and temperature.

Methods. We use MoCA (Monte Carlo code for Comptonisation in Astrophysics) to produce synthetic spectra for the case of an AGN with $M_{\text{BH}} = 1.5 \times 10^8 M_{\odot}$ and $\dot{m} = 0.1$ and then compared them with the widely used power-law model with an exponential high-energy cutoff.

Results. We provide phenomenological relations relating Γ and E_c with the opacity and temperature of the coronal electrons for the case of spherical and slab-like coronae. These relations give origin to a well defined parameter space which fully contains the observed values. Exploiting the increasing number of high-energy cut-offs quoted in the literature, we report on the comparison of physical quantities obtained using MoCA with those estimated using commonly adopted spectral Comptonisation models. Finally, we discuss the negligible impact of different black hole masses and accretion rates on the inferred relations.

Key words. galaxies: active – quasars: general – X-rays: galaxies

1. Introduction

X-rays emerging from active galactic nuclei (AGNs) are the result of an inverse-Compton process occurring in the proximity of the central black hole (BH), where optical-UV photons arising from the accretion disc are inverse-Compton scattered by hot electrons in an optically thin, compact corona (e.g. Haardt & Maraschi 1991, 1993; Haardt et al. 1994, for details on the two-phase model). Such a Comptonisation mechanism accounts for the power-law-like shape of the X-ray primary continuum emission and the high-energy roll-over observed in various nearby AGNs (e.g. Nicastro et al. 2000; Perola et al. 2002; De Rosa et al. 2002; Molina et al. 2009, 2013; Malizia et al. 2014; Ricci et al. 2018). Broadband X-ray spectral investigations are of primary importance in studying AGN Comptonisation properties. Indeed, as extensively discussed in the literature (e.g. Ghisellini 2013) both the photon index (Γ) and high-energy cut-off (E_c) of the X-ray primary emission depend on the intrinsic properties of the Comptonising medium, namely its temperature, optical depth, and geometry. Therefore, the interplay between coronal parameters and the AGN X-ray spectral shape has been the object of several investigations, especially with observatories capable of detecting hard X-rays. Dadina

(2007), using *BeppoSAX* data, collected and studied the photon index and E_c of a sample of AGNs (see also Perola et al. 2002, for previous results), while similar works were performed on INTEGRAL data (e.g. Bassani et al. 2006; Molina et al. 2009; Malizia et al. 2014), and, in the context of the BAT AGN Spectroscopic Survey, by Ricci et al. (2018). Subsequently, *NuSTAR* (Harrison et al. 2013), thanks to its unprecedented effective area above 10 keV, greatly helped in studying the exponential cut-offs of the nuclear continuum in several AGNs (see e.g. Fabian et al. 2015, 2017; Tortosa et al. 2018a). These space missions gave rise to a substantial corpus of high-energy cut-off and photon index measurements.

While several Comptonisation models exist in the literature, many of them also available for direct fitting to the data, they are usually valid in a limited range of parameters. Moreover, in some papers, especially in the past and/or when a large sample of sources were analysed, only the phenomenological parameters are provided. It could therefore be of some help to have relations converting phenomenological parameters to physical ones. Petrucci et al. (2000) provided an approximate relation between the observed high-energy cut-off of NGC 5548 and the thermal energy of the corona ($E_c \sim 2-3 kT$), while Petrucci et al. (2001) discussed this for a larger sample of Seyfert 1 galaxies observed

with *BeppoSAX*. However, this relation has proven to be accurate only for an extended slab geometry. On the other hand, [Beloborodov \(1999\)](#) reports a relation between the spectral photon index and the Compton parameter y . This parameter is the product of the average fractional energy change per scattering and the mean number of scatters that the photon undergoes. Subsequently, y is used to characterise the energy gain of a photon scattering within a finite medium. The Compton parameter encodes the physical conditions of the coronal plasma, and it can be defined as follows:

$$y = 4(\theta + 4\theta^2)\tau(\tau + 1), \quad (1)$$

where $\theta = kT/m_e c^2$, and τ is the Comptonising medium opacity. Furthermore, [Beloborodov \(1999\)](#) found that the photon index is related to y according to $\Gamma \approx \frac{4}{9} y^{-2/9}$.

In this paper, we derive and discuss formulae which directly relate the phenomenological quantities Γ - E_c with the corresponding coronal properties kT - τ for the cases of a slab-like and spherical corona. These relations were obtained using MoCA (Monte Carlo code for Comptonisation in Astrophysics, [Tamborra et al. 2018](#)).

2. MoCA simulations and setup

2.1. Hot corona and accretion disc

Comptonisation Monte Carlo code (MoCA; see [Tamborra et al. 2018](#) for a detailed description of the code) is based on a single photon approach, working in a fully special relativistic scenario. MoCA allows for various and different physical and geometrical conditions of the accretion disc and of the Comptonising corona. In this paper, the corona is assumed to have either a spherical or a slab-like geometry, and to be as extended as the disc, whose radii have been set to be $R_{\text{out}} = 500 r_g$ and $R_{\text{in}} = 6 r_g$, respectively. Even though arguments (e.g. variability, [Uttley et al. 2014](#), and references therein, microlensing [Chartas et al. 2009](#); [Morgan et al. 2012](#) and timing [Kara et al. 2016](#); [De Marco et al. 2013](#)) exist that favour a compact corona, we used extended coronae. In fact, as discussed by [Marinucci et al. \(2019\)](#), Comptonised spectra emerging from compact corona ($R_{\text{out}} = 100 r_g$, $R_{\text{in}} = 6$) do not deviate significantly from those produced in more extended corona; see their Fig. 3. The adoption of even more compact coronae ($R_{\text{out}} = 20 r_g$, $R_{\text{in}} = 6$) results only in the need for higher optical depths to recover the same spectral shape for a given temperature. However, in such cases, general relativity (GR) effects are not negligible (see [Tamborra et al. 2018](#), for a detailed discussion on this topic), and the present version of MoCA does not include GR. For the slab-like geometry case, MoCA allows the user to set up the corona height above the accretion disc (set to $10 r_g$ in our simulations). We use synthetic spectra computed assuming the source BH mass and accretion rate to be the same as those of Ark 120 (e.g. [Marinucci et al. 2019](#), and references therein), namely $M_{\text{BH}} = 1.5 \times 10^8 M_\odot$ and $\dot{m} = L_{\text{bol}}/L_{\text{Edd}} = 0.1$. For both the slab and spherical hot electron configurations, we simulated the Comptonised spectra using a wide range of values for electron temperature and optical depth: $0.1 < \tau < 7$ and $20 < kT < 200$ keV, and in Fig. 1 we show a sample of spectra obtained by MoCA. Moreover, spectra are computed from 0.01 keV up to 700 keV using 1000 logarithmic energy bins, and a Poissonian error accompanies each spectral point. The obtained spectra are averaged over the inclination angle and in Fig. 1 we show some exemplificative spectra normalised at 1 keV accounting for the two geometries considered in this work.

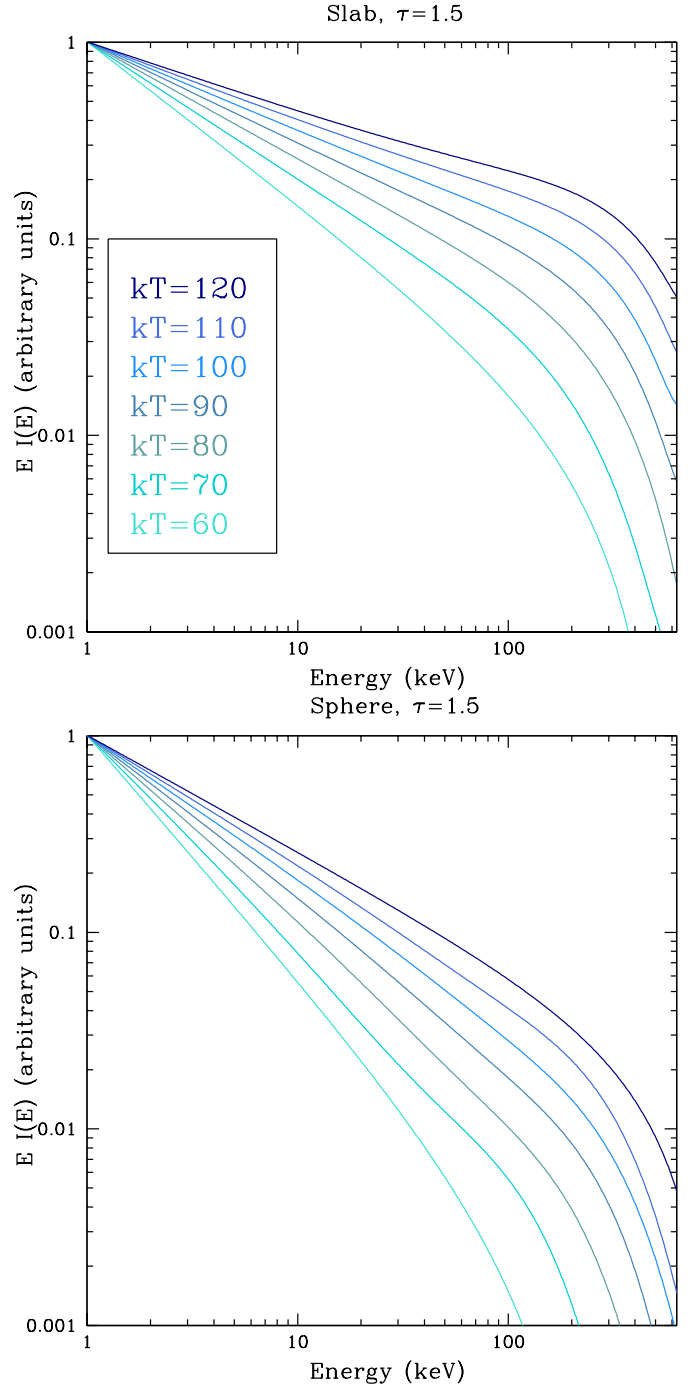


Fig. 1. $E I(E)$ graphs of the MoCA simulations normalised at 1 keV. Curves refer to a fixed $\tau = 1.5$ and different electron temperatures. The colour code is the same for the two panels. It is worth noting that the same τ - kT couple gives rise to different spectra when the slab-like or the spherical geometries are considered.

2.2. Analysis

To find relations between the phenomenological and physical coronal parameters, we fitted the simulated spectra with a power law with an exponential cut-off (model *cutoffpl* in *Xspec*, [Arnaud 1996](#)). During the fitting procedure, the high-energy cut-off, the normalisation, and the photon index of the primary continuum emission are free to vary. Fits are performed in the 2–700 keV energy interval, or up to the last populated energy bin, if lower than 700 keV. In the fits, the C statistic has been used

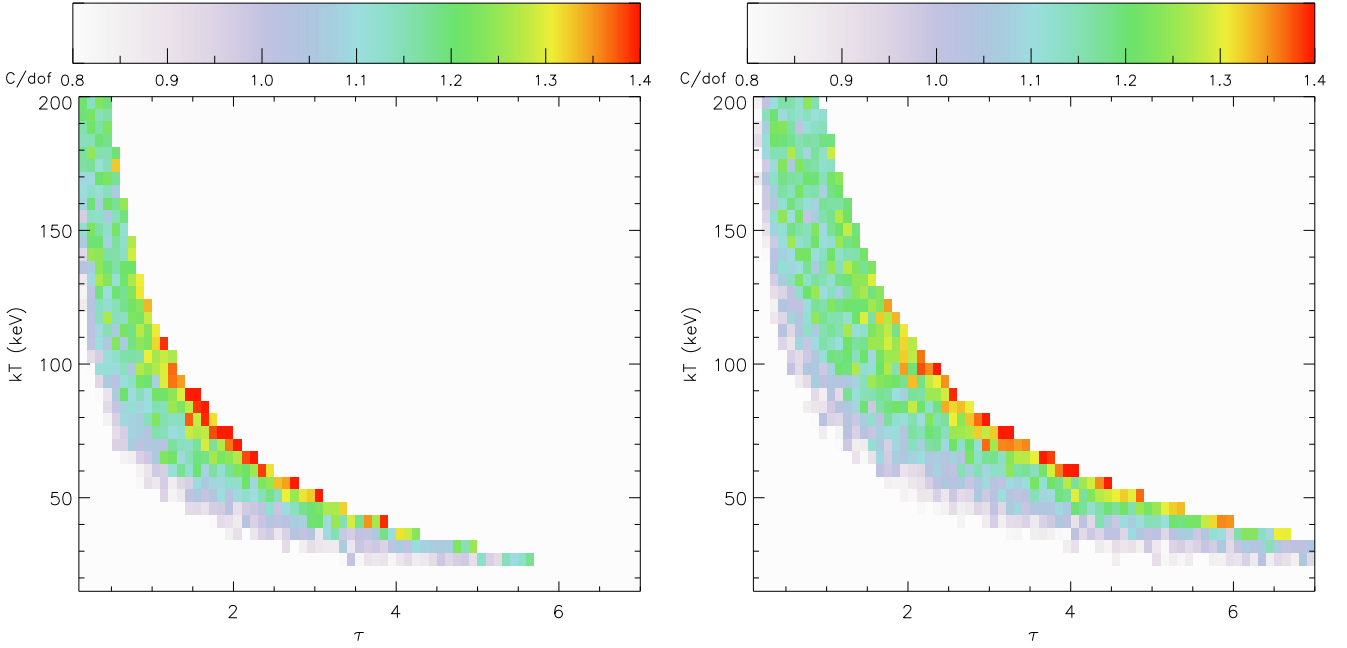


Fig. 2. Map of the ratios between the C statistics and the degrees of freedom for the slab-like (*left*) and spherical (*right*) cases. The cut-off power law is a good approximation of the simulated spectra.

(Cash 1979). These steps yield a corresponding fitted Γ - E_c pair for each kT - τ couple. At this stage of the analysis, we excluded all the spectra for which we obtained a photon index outside the interval 1.5–2.5. In fact, we have no evidence of AGNs with such a flat or steep photon index (e.g. Bianchi et al. 2009; Sobolewska & Papadakis 2009; Serafinelli et al. 2017). In general, the cut-off power law is a very good approximation of the simulated spectra and in Fig. 2 we show the goodness of the fits (quantified in terms of the $C/d.o.f.$ ratio) as a function of the coronal properties. We notice that this ratio increases towards those regions corresponding to photon indices as flat as ~ 1.5 and residuals with respect the cut-off power law mainly occur at high energy; see Fig. 3. These high-energy residuals cannot be observed with current facilities; indeed, they are outside the bandpass of the major operating observatories, and when instruments are sensible to such energetic photons these deviations are not detectable with the available signal-to-noise ratio.

To derive relations connecting Γ - E_c with kT - τ , we started analysing the dependence of the photon index on the Compton parameter y . For each Γ - E_c couple, we then computed the corresponding y using the proper τ - kT . In Fig. 4, we plot the photon index as a function of y for different values of τ and for a fixed kT . We then performed log-log fits between Γ and y . In the fits, both the normalisation and the slope are free to vary. These Γ and the Compton parameter y are clearly correlated, although points are widely dispersed; see Fig. 4. On the other hand, we found that such a widespread dispersion is due to a further dependence of Γ on the coronal temperature, which we quantified studying how the slopes (a) and normalisations (b) of the fits behave as a function of kT . We then performed additional fits between the following parameters: $a - kT$ and $b - kT$. This procedure leads to Eq. (2) for the case of a slab-like corona:

$$\begin{aligned} \log \Gamma(\theta, \tau) &= a(\theta) \log y(\theta, \tau) + b(\theta) \\ a(\theta) &= -0.34 + 1.02 \times \theta - 1.46 \times \theta^2 \\ b(\theta) &= 0.47 - 1.02 \times \theta + 1.64 \times \theta^2, \end{aligned} \quad (2)$$

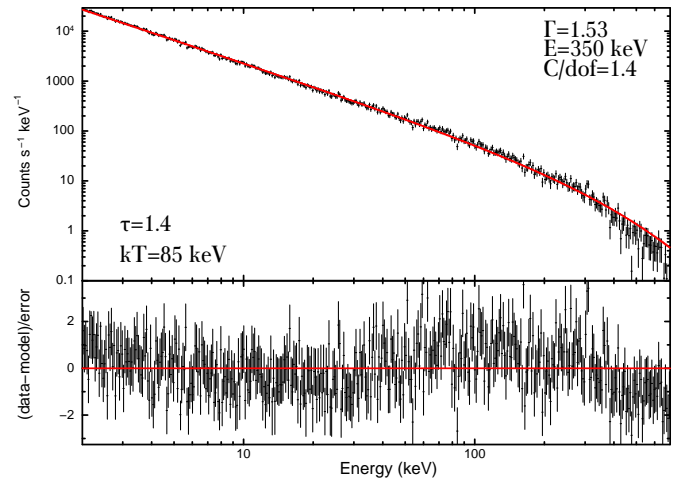


Fig. 3. Case of a spectrum with a relatively high $C/d.o.f.$ emerging from a slab corona with $\tau = 1.4$ and $kT = 85$ keV. The cut-off power law leaves residuals mainly above 100 keV.

where $\theta = \frac{kT}{m_e c^2}$. For the spherical case we obtain

$$\begin{aligned} \log \Gamma(\theta, \tau) &= a(\theta) \log y(\theta, \tau) + b(\theta) \\ a(\theta) &= -0.35 + 0.87 \times \theta - 1.04 \times \theta^2 \\ b(\theta) &= 0.60 - 1.53 \times \theta + 1.83 \times \theta^2. \end{aligned} \quad (3)$$

In accordance with these formulae, the photon index does not depend only on y , but is rather a function of kT and y . To estimate the associated mean uncertainty $\Delta\Gamma/\Gamma$ for Eqs. (2) and (3) we compared the inferred photon indices with values obtained fitting the simulations. The average of all the percentage errors yields a $\Delta\Gamma/\Gamma$ of $\sim 1.5\%$ (1%) for the case of a slab-like (spherical) hot-corona. For the case of spherical geometry, we compared our Eq. (3) with the relation by Beloborodov (1999): $\Gamma \approx \frac{4}{9} y^{-2/9}$. The author computed his equation by studying spectra simulated with the code

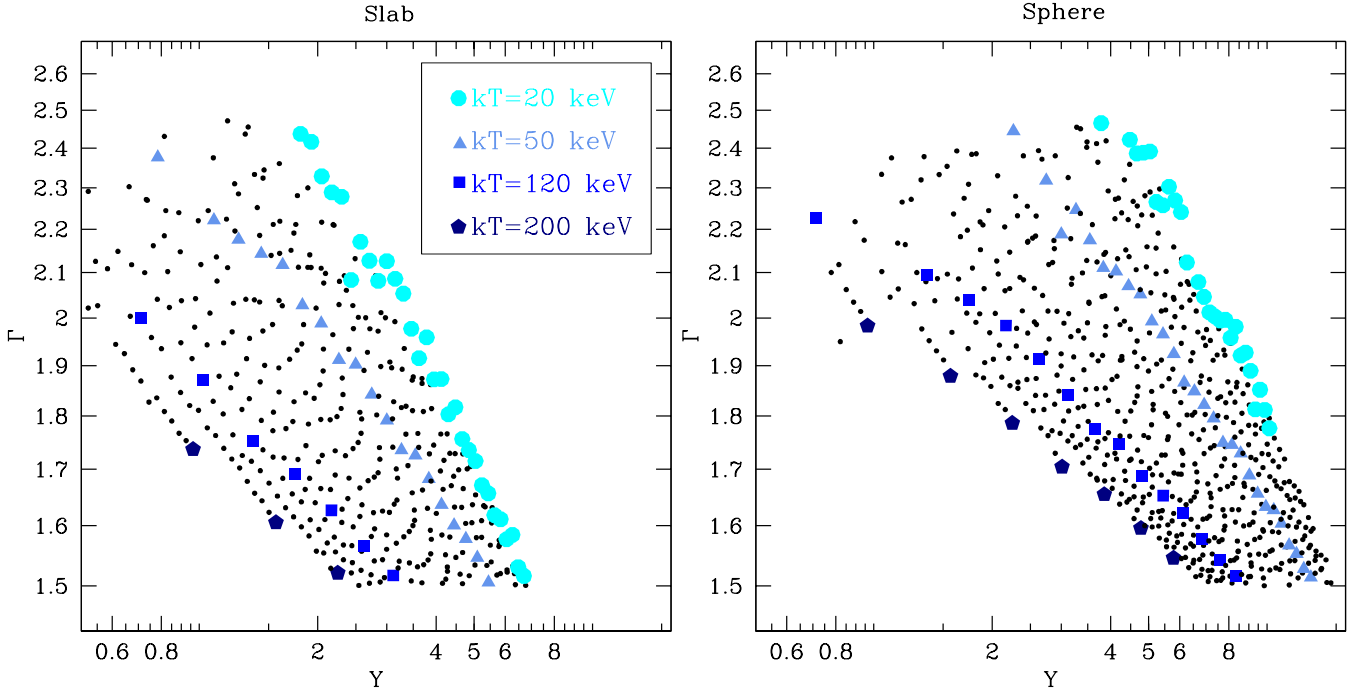


Fig. 4. Photon index as a function of the Compton parameter. The y parameter is computed for the various optical depths and for all the temperatures (kept fixed). The colour code is the same for both panels.

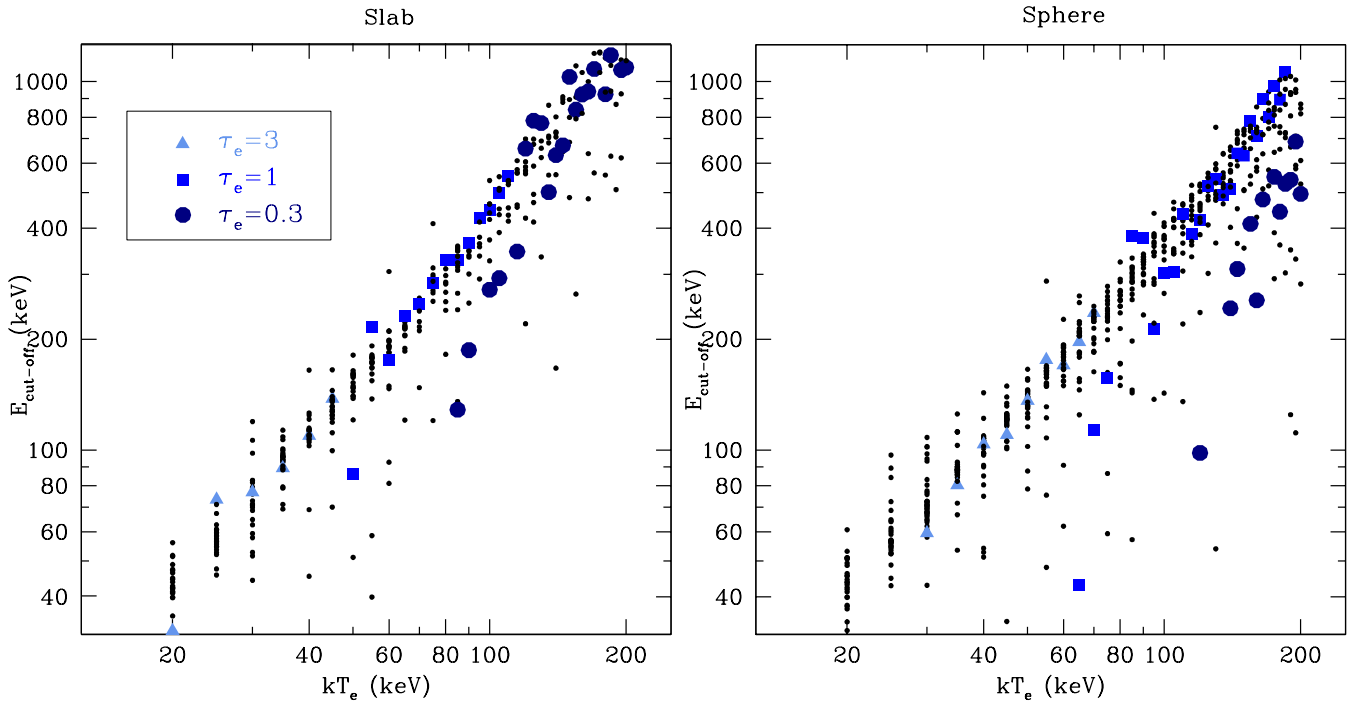


Fig. 5. High-energy cut-off as a function of the electron temperature, for a fixed optical depth. Colours are the same in both graphs.

by Coppi & Zdziarski (1992) for only two values of kT (50 and 100 keV) and leaving the electron opacity free to vary. To estimate its uncertainty, we calculated the expected photon index using the relation by Beloborodov (1999) for all the kT - τ couples. The comparison of these estimates with the fitted Γ leads to an average percentage uncertainty of $\Delta\Gamma/\Gamma = 14\%$, showing that this simplified formula significantly deviates from the MoCA predictions.

In a similar fashion, we derived relations connecting the high-energy cut-off with the physical properties of the Comp-

tonising plasma. The high-energy roll-over is mainly dependent on the coronal temperature. Thus, we started studying the E_c as a function of kT keeping τ fixed; see Fig. 5. The dependence of E_c on the plasma temperature is estimated by performing log-log fits between this parameter and kT for different values of τ . On the other hand, the obtained slopes (α) and normalisations (β) are found to depend on the coronal opacity. Therefore, we quantified this dependence on the optical depth by performing linear fits for α and β as a function of τ . For the case of a slab-like

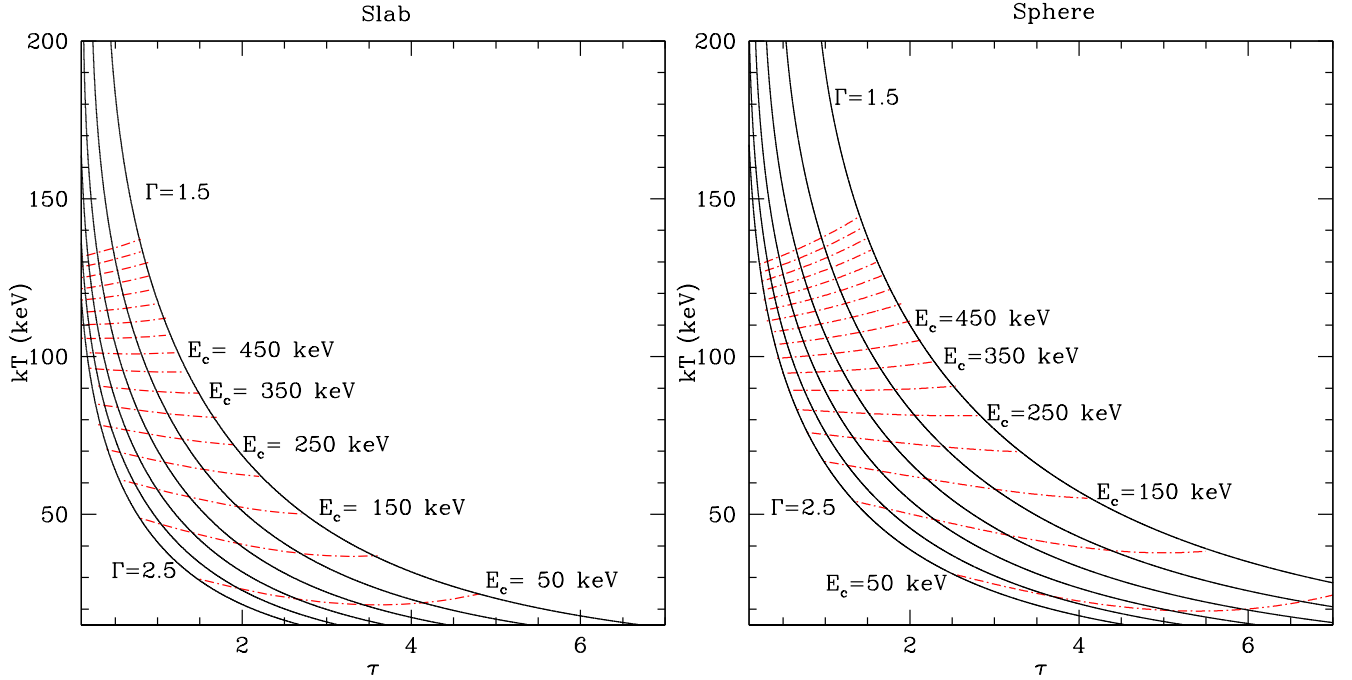


Fig. 6. Grids in the physical parameters space computed using Eqs. (2)–(5). Black solid lines represent the iso- Γ curves, while iso- E_c are shown via the red solid-dashed lines. Iso- Γ curves have a 0.2 step and Γ steepens from right to left. A 50 keV step is used to represent the various high-energy cut-off iso-curves.

corona these steps yield the following relations:

$$\begin{aligned} \log \frac{E_c}{\text{keV}} &= \alpha(\tau) \times (\log \theta + 2.71) + \beta(\tau) \\ \alpha(\tau) &= 2.48 - 0.57 \times \tau + 0.065 \times \tau^2 \\ \beta(\tau) &= -2.33 + 1.16 \times \tau - 0.14 \times \tau^2. \end{aligned} \quad (4)$$

For a spherical geometry we obtain

$$\begin{aligned} \log \frac{E_c}{\text{keV}} &= \alpha(\tau) \times (\log \theta + 2.71) + \beta(\tau) \\ \alpha(\tau) &= 2.98 - 0.66 \times \tau + 0.054 \times \tau^2 \\ \beta(\tau) &= 3.35 + 1.3 \times \tau - 0.11 \times \tau^2. \end{aligned} \quad (5)$$

The uncertainty associated with Eq. (4) is $\Delta E_c/E_c \simeq 13\%$, while for the case of a spherical corona we obtain $\Delta E_c/E_c \simeq 17\%$. For both geometries considered here, the high-energy cut-off not only depends on the electron temperature, but also on the coronal opacity. The above equations directly relate the high-energy cut-off with the coronal temperature and encode the dependence on opacity of the Comptonising electrons.

Once the dependence between the phenomenological parameters and the physical kT and τ have been quantified, we use Eqs. (2) and (4) for the slab-like coronae and Eqs. (3) and (5) for the spherical coronae to determine the interesting regions in the kT - τ parameters space. In particular, by plotting iso- Γ curves for $1.5 \leq \Gamma \leq 2.5$ and iso- E_c lines, we identify regions in the physical parameters plane corresponding to typically measured AGN photon indices and high-energy cut-offs; see Fig. 6. On average, for a certain Γ , a slab corona returns lower values of optical depth and temperature, while to reach the same spectral shape, higher kT and τ are required when a sphere-like corona is considered. Moreover, iso- E_c curves behave differently for the two geometries. Indeed for the sphere, high-energy cut-offs generally correspond to higher temperatures ($\gtrsim 10$ keV more) if compared with those measured assuming a slab corona. Furthermore, we

observe that the commonly adopted relation $E_c \sim 2-3 kT$ is not valid for all the kT and τ regimes; see Fig. 7.

In this figure, we show the high-energy cut-off and electron temperature ratio as a function of the coronal opacity. In particular, we point out that for low-temperature regimes the optical depth does not play any role in determining the cut-off energy of the spectrum, while at larger electron temperatures, the E_c/kT ratio is no more insensitive to the coronal opacity.

Since a dependence of the Comptonised spectra on the spectral shape of the seed photons would affect our conversions and the derived coronal parameters, here we check if Eqs. (2)–(5) can be broadly used regardless of the AGN black hole mass and accretion rate. We computed simulations for $M_{\text{BH}} = 10^7 M_\odot$ and $\dot{m} = 0.1$, $M_{\text{BH}} = 10^8 M_\odot$ with $\dot{m} = 0.05$ and $\dot{m} = 0.2$, and, finally, for $M_{\text{BH}} = 10^9 M_\odot$ and $\dot{m} = 0.1$. Following the same procedure described in Sect. 3, we fitted these spectra using a cut-off power-law model within *Xspec*. As in the previous case, this allowed us to build a new database of correspondences between the phenomenological and physical parameters. Neither the photon index nor the high-energy cut-off estimates are strongly dependent on the particular values of black hole masses and accretion rate. In fact, we notice that the fitted values for the phenomenological parameters are within the uncertainties associated to the equations reported in this section.

3. Estimates of coronal parameters in local AGNs

3.1. The NuSTAR sample

Our relations can be used for probing the coronal properties of AGNs. From Eqs. (2)–(5), we can directly obtain the coronal properties of those Seyfert galaxies for which E_c and Γ are available. Here, we consider the AGN sample presented by Tortosa et al. (2018a), which we updated to include recently observed AGNs. Moreover, when multiple values are found in the literature for the same source, Γ and E_c measurements based on broadband analyses have been preferred. The use of our

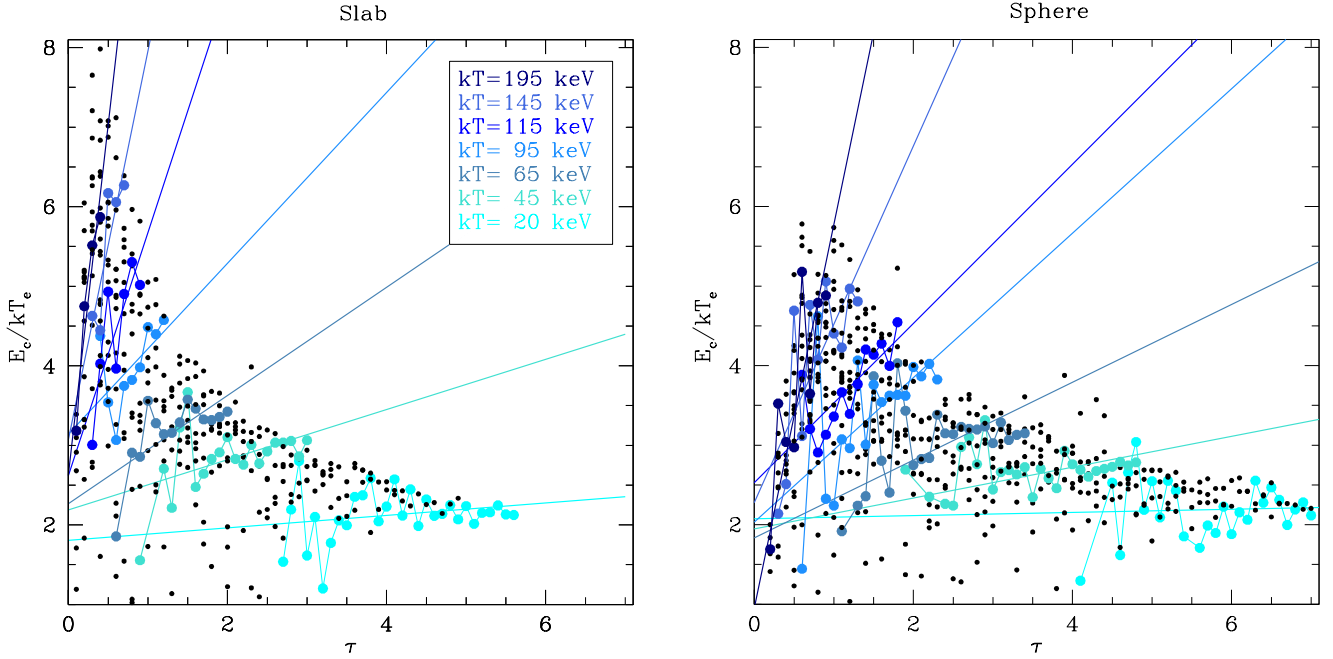


Fig. 7. Ratio between the high-energy cut-off E_c and the coronal temperature kT displayed as a function of the optical depth τ for both geometries. In both panels, straight solid lines represent the best-fit between E_c/kT and τ at a fixed temperature kT , while lines connecting the points are reported for plot purposes only.

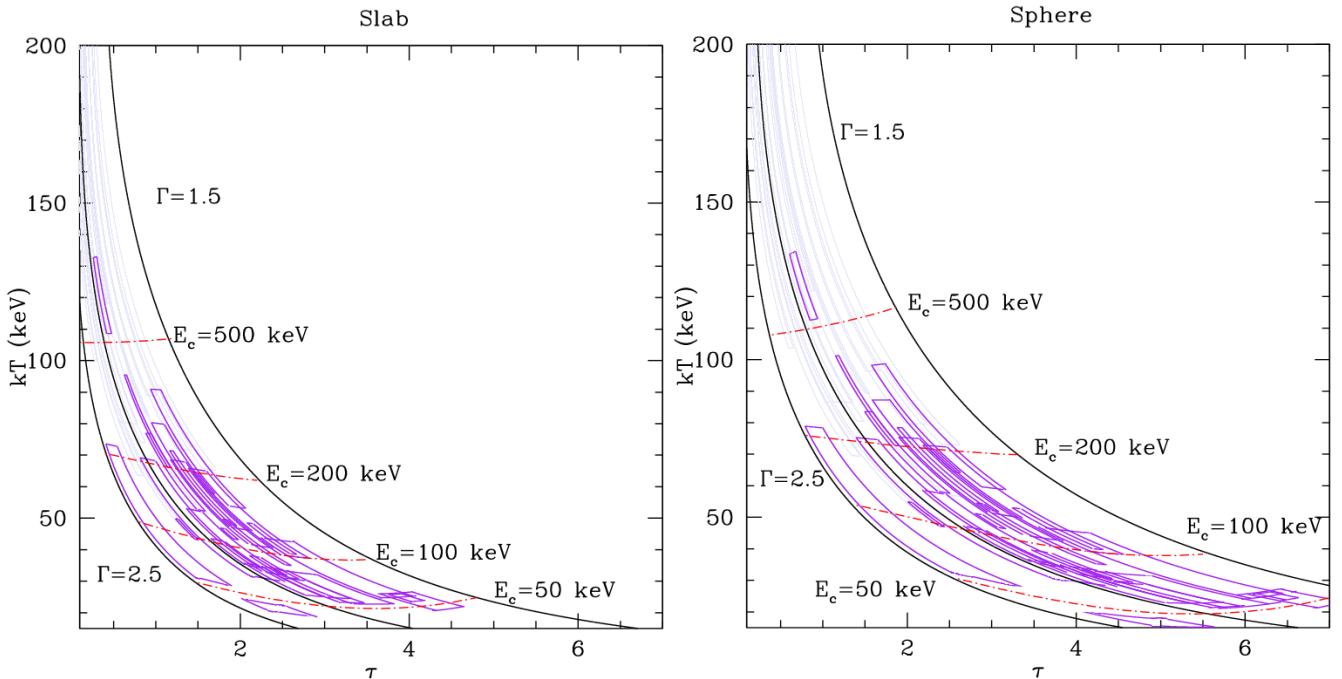


Fig. 8. Contours in the physical parameter space for all the AGNs reported in Table 1. Magenta contours correspond to measured high-energy cut-off while blue is used for AGNs characterised by an unconstrained high-energy cut-off. Moreover, black and red curves emphasise the iso- Γ and iso- E_c labelled in the plot.

formulae on the chosen phenomenological parameters Γ and E_c yielded Table 1, in which we report the MoCA-based estimates for the coronal optical depth and temperature.

As expected, the optical depths for the slab-like coroneae are systematically smaller than those derived assuming a spherical corona (see Table 1, Figs. 1 and 6). This is due to the fact that in the spherical corona the optical depth τ is the radial one, and is therefore the same in all directions, while for the slab-case τ is the vertical and therefore minimal value. Adopting the

equations derived in Sect. 2, we compute contour plots of the sources listed in Table 1; see Fig. 8. When the source high-energy cut-off is well determined, the corresponding contour in the physical parameter space is closed (see purple contours in Fig. 8), otherwise the corresponding curves are not limited at high kT (lavender in Fig. 8). The average values for the coronal opacity and temperature are $\tau = 1.9 \pm 0.8$, $kT = 50 \pm 21$ keV and $\tau = 3.1 \pm 1.3$, $kT = 53 \pm 23$ keV for the slab-like and the spherical geometries, respectively. We obtain a larger τ and a smaller

Table 1. MoCA estimates for various AGNs observed by *NuSTAR* characterised by $N_{\text{H}} < 6 \times 10^{22} \text{ cm}^{-2}$.

Source name	Γ	$E_{\text{cut-off}}$ (keV)	References	Slab		Sphere	
				kT (keV)	τ	kT (keV)	τ
Ark 564	2.27 ± 0.08	42 ± 3	1	21^{+2}_{-2}	$2.4^{+0.4}_{-0.3}$	17^{+2}_{-1}	$5.0^{+0.6}_{-0.6}$
GRS 1734–292	1.65 ± 0.05	53^{+11}_{-8}	2	23^{+3}_{-2}	$4.2^{+0.5}_{-0.6}$	24^{+3}_{-2}	$6.7^{+0.7}_{-0.7}$
NGC 3783	1.87 ± 0.04	63^{+11}_{-8}	3	26^{+4}_{-3}	$3.0^{+0.5}_{-0.5}$	24^{+4}_{-3}	$5.3^{+0.7}_{-0.9}$
B1422+231	$1.81^{+0.07}_{-0.06}$	66^{+17}_{-12}	4	26^{+8}_{-3}	$3.2^{+0.6}_{-0.8}$	25^{+7}_{-4}	$5.4^{+0.8}_{-1.4}$
ESO141-G55	1.94 ± 0.03	69^{+14}_{-10}	3	30^{+6}_{-5}	$2.5^{+0.4}_{-0.4}$	28^{+8}_{-5}	$4.5^{+0.8}_{-1.0}$
Mrk 348	1.68 ± 0.05	79^{+39}_{-19}	3	31^{+12}_{-6}	$3.3^{+0.8}_{-1.0}$	30^{+15}_{-5}	$5.4^{+1.2}_{-1.8}$
4U 1344–60	1.95 ± 0.03	91^{+13}_{-10}	3	39^{+5}_{-4}	$1.9^{+0.3}_{-0.3}$	40^{+6}_{-6}	$3.2^{+0.5}_{-0.5}$
PG 1247+267	2.33 ± 0.1	96^{+130}_{-37}	5	46^{+28}_{-14}	$1.0^{+0.7}_{-0.6}$	51^{+28}_{-18}	$1.7^{+1.3}_{-0.9}$
Mrk 1040	1.91 ± 0.04	99^{+39}_{-22}	3	41^{+12}_{-8}	$1.9^{+0.6}_{-0.6}$	43^{+14}_{-12}	$3.1^{+1.2}_{-0.9}$
2MASSJ1614346+470420	$1.98^{+0.11}_{-0.05}$	106^{+102}_{-37}	4	44^{+26}_{-11}	$1.6^{+0.8}_{-0.7}$	48^{+26}_{-20}	$2.6^{+1.4}_{-1.2}$
NGC 3998	1.79 ± 0.01	107^{+27}_{-18}	6	41^{+8}_{-6}	$2.2^{+0.4}_{-0.4}$	43^{+11}_{-8}	$3.5^{+0.8}_{-0.7}$
SWIFT J2127.4+5654	2.08 ± 0.01	108^{+11}_{-10}	7	46^{+3}_{-3}	$1.4^{+0.1}_{-0.1}$	51^{+4}_{-4}	$2.2^{+0.2}_{-0.2}$
MCG -05-23-16	1.85 ± 0.01	116^{+6}_{-5}	8	45^{+2}_{-2}	$1.9^{+0.1}_{-0.1}$	49^{+2}_{-2}	$3.0^{+0.2}_{-0.2}$
3C390.3	1.71 ± 0.01	117^{+18}_{-14}	9	43^{+5}_{-4}	$2.3^{+0.3}_{-0.3}$	46^{+7}_{-6}	$3.7^{+0.5}_{-0.5}$
Mrk 509	1.78 ± 0.04	143^{+72}_{-36}	3	52^{+16}_{-10}	$1.8^{+0.6}_{-0.6}$	57^{+18}_{-13}	$2.8^{+1.0}_{-0.8}$
NGC 6814	$1.71^{+0.04}_{-0.03}$	155^{+70}_{-35}	10	54^{+15}_{-10}	$1.8^{+0.5}_{-0.6}$	60^{+17}_{-12}	$2.9^{+0.9}_{-0.8}$
NGC 7469	1.78 ± 0.02	170^{+60}_{-40}	11	59^{+12}_{-10}	$1.5^{+0.4}_{-0.4}$	65^{+13}_{-12}	$2.4^{+0.7}_{-0.5}$
NGC 4593	1.69 ± 0.02	170^{+160}_{-60}	12	57^{+29}_{-17}	$1.8^{+0.8}_{-0.8}$	63^{+30}_{-21}	$2.8^{+1.4}_{-1.1}$
MCG +8-11-11	1.77 ± 0.04	175^{+110}_{-50}	10	60^{+20}_{-13}	$1.5^{+0.6}_{-0.6}$	66^{+21}_{-15}	$2.4^{+0.9}_{-0.8}$
Ark 120	1.87 ± 0.02	183^{+83}_{-43}	13	63^{+14}_{-10}	$1.2^{+0.3}_{-0.4}$	69^{+15}_{-11}	$2.0^{+0.5}_{-0.5}$
IC4329A	1.73 ± 0.01	186 ± 14	14	62^{+3}_{-3}	$1.6^{+0.1}_{-0.1}$	68^{+3}_{-4}	$2.4^{+0.2}_{-0.2}$
NGC 4151	1.63 ± 0.04	196^{+47}_{-32}	15	62^{+9}_{-8}	$1.8^{+0.4}_{-0.4}$	70^{+10}_{-8}	$2.7^{+0.6}_{-0.5}$
3C382	$1.68^{+0.03}_{-0.02}$	214^{+147}_{-63}	16	67^{+23}_{-14}	$1.5^{+0.5}_{-0.6}$	74^{+23}_{-15}	$2.4^{+0.8}_{-0.8}$
M 81	1.86 ± 0.01	220^{+173}_{-86}	17	70^{+17}_{-12}	$1.1^{+0.6}_{-0.4}$	77^{+23}_{-21}	$1.8^{+0.8}_{-0.6}$
3C 120	1.87 ± 0.02	305^{+142}_{-74}	15	83^{+17}_{-12}	$0.8^{+0.2}_{-0.3}$	90^{+15}_{-11}	$1.4^{+0.3}_{-0.3}$
NGC 5506	1.91 ± 0.03	720^{+130}_{-190}	18	123^{+9}_{-15}	$0.3^{+0.1}_{-0.1}$	127^{+8}_{-15}	$0.7^{+0.2}_{-0.2}$
MCG 6-30-15	2.061 ± 0.005	>110	19	>47	<1.4	>51	<2.2
NGC 7213	1.84 ± 0.03	>140	20	>52	<1.7	>57	<2.6
Mrk 335	$2.14^{+0.02}_{-0.04}$	>174	21	>64	<0.9	>70	<1.5
NGC 2110	1.65 ± 0.03	>210	22	>66	<1.7	>73	<2.6
Fairall9	$1.96^{+0.01}_{-0.02}$	>240	23	>74	<0.9	>81	<1.5
ESO 362-G18	$1.71^{+0.03}_{-0.05}$	>241	3	>72	<1.4	>80	<2.2
HE 0436–4717	2.01 ± 0.08	>280	24	>80	<0.8	>86	<1.3
NGC 4579	1.81 ± 0.01	>299	6	>82	<0.9	>89	<1.6
NGC 2992	1.72 ± 0.03	>350	25	>90	<1.0	>96	<1.7
Mrk 766	2.22 ± 0.03	>350	26	>90	<0.4	>94	<0.8

Notes. The first column identifies the source while in Cols. 2 and 3 the literature values for the photon index and the high energy cut-off are given. In column number 4 we report the bibliographic references for the phenomenological parameters. Then in Cols. 5 and 6 (7 and 8) we report the MoCA τ - kT estimates for the slab (sphere) geometry. Positive(negative) errors are estimated by applying our equations on the nominal phenomenological parameter value plus (minus) its associated uncertainty.

References. (1) Kara et al. (2017); (2) Tortosa et al. (2017); (3) Rani et al. (2019); (4) Lanzuisi et al. (2019); (5) Lanzuisi et al. (2016); (6) Younes et al. (2019); (7) Marinucci et al. (2014a); (8) Baloković et al. (2015); (9) Lohfink et al. (2015); (10) Tortosa et al. (2018b); (11) Middei et al. (2018a); (12) Ursini et al. (2016); (13) Porquet et al. (2018); (14) Brenneman et al. (2014); (15) Fabian et al. (2017); (16) Ballantyne et al. (2014); (17) Young et al. (2018); (18) Matt et al. (2015); (19) Marinucci et al. (2014b); (20) Ursini et al. (2015); (21) Parker et al. (2014); (22) Marinucci et al. (2015); (23) Lohfink et al. (2016); (24) Middei et al. (2018b); (25) Marinucci et al. (2018); (26) Risaliti et al. (2011), Buisson et al. (2018).

kT than the ones presented in Ricci et al. (2018), for a slab-like geometry; likely because they included upper limits on the optical depth and lower limits of high-energy cut-off. Moreover, these latter authors computed kT to be $E_c/2$, thus overestimating the electron temperature, especially at low opacity; see Fig. 7.

3.2. Comparison with different comptonisation codes

As a further step, we compared our estimates with those in literature. In particular, in Fig. 9, we compare the MoCA-based estimates with those reported by other authors and resulting from spectroscopic analyses based on various Comptonisation codes

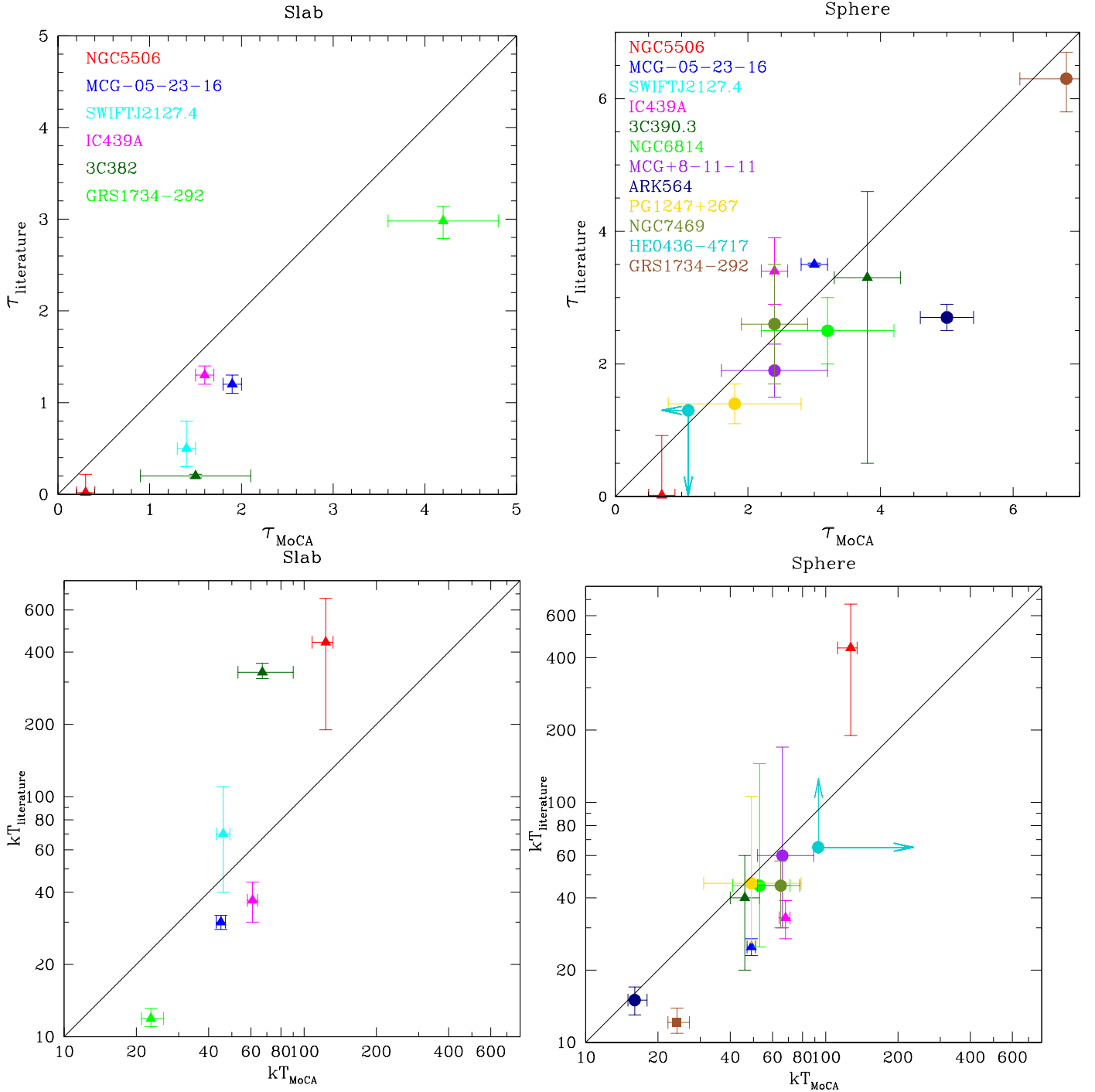


Fig. 9. Comparison of estimates of kT and τ obtained with MoCA and using different models: *nthcomp* (triangles), *compTT* (circles), and *compPS* (squares); see Tortosa et al. (2018a) and references therein. The 1:1 relation to the graph is also shown. The top and bottom left panels are computed for a slab-like corona, while the remaining panels account for the spherical case. Different coloured names correspond to the various sources that are the same between top and bottom left panels and top and bottom right panels. Temperature and optical depth literature values for the sources are reported by Tortosa et al. (2018a), with the exception of NGC 7469 and HE 0436–4714 for which kT and τ are reported by Middei et al. (2018a,b), respectively.

(i.e. *compTT* Titarchuk 1994, *nthcomp* Zdziarski et al. 1996, and *compPS* Poutanen & Svensson 1996). MoCA-measurements of the slab-like coronal opacity appear to be larger, on average, than τ obtained with other models (see top left panel of Fig. 9), while no trend is found between MoCA and literature values of the electron temperature. For the spherical case, MoCA estimates of the coronal opacity and electron temperature, except for a few

exceptions (e.g. NGC 5506), are compatible with measurements from *compTT*, *nthcomp*, and *compPS*.

4. Summary and conclusion

This paper reports on the first systematic application of the code MoCA (Tamborra et al. 2018) to study the high-energy emission

of AGNs. MoCA allowed us to simulate X-ray spectra assuming a wide range of parameters describing the AGNs (M_{BH} , m) as well as the Comptonising medium, such as geometry, temperature, and optical depth. The main results can be summarised as follows:

- We derived relations between phenomenological (Γ and E_c) and physical (electron temperature and optical depth) coronal parameters, assuming either a spherical corona or a slab-like one. We find that Γ depends on the Compton parameter y , and also on kT . The E_c is a function of the coronal temperature and the optical depth; see Eqs. (2)–(5), and Fig. 7. Moreover, the relation $E_c = 2-3kT$ is found to be valid only for a limited range of physical parameters, especially for low τ and kT ; see Fig. 7.
- The derived equations allowed us to determine the loci occupied by the observed AGNs in the physical space of the electron temperature and optical depth (see Fig. 6), resulting in a plot useful for deriving the AGN coronal properties from the measured Γ and E_c . We then applied the results to an upgraded version of the AGN sample of Tortosa et al. (2018a). We found the impact of the seed photon field spectral shape on the emerging Comptonised spectrum to be weak. The Γ - E_c measurements obtained for different black hole masses and accretion rates are consistent within the dispersion with those estimated using Eqs. (2)–(5).

Acknowledgements. We thank the referee for her/his comments. RM acknowledges Fausto Vagnetti for his precious informatic support, Fondazione Angelo Della Riccia for financial support, Université Grenoble Alpes and the high energy SHERPAS group for welcoming him at IPAG. Pop acknowledges financial support by the CNES and the Programme National High Energies (PNHE) of CNRS/INSU with INP and IN2P3, co-funded by CEA and CNES. FT acknowledges financial support by CAMK and the project “Modelling the X-ray spectral-timing properties of accreting BH systems with realistic Comptonisation models” (PI: Barbara De Marco).

References

- Arnaud, K. A. 1996, in *Astronomical Data Analysis Software and Systems V*, eds. G. H. Jacoby, & J. Barnes, *ASP Conf. Ser.*, 101, 17
- Ballantyne, D. R., Bollenbacher, J. M., Brenneman, L. W., et al. 2014, *ApJ*, 794, 62
- Baloković, M., Matt, G., Harrison, F. A., et al. 2015, *ApJ*, 800, 62
- Bassani, L., Molina, M., Malizia, A., et al. 2006, *ApJ*, 636, L65
- Beloborodov, A. M. 1999, in *High Energy Processes in Accreting Black Holes*, eds. J. Poutanen, & R. Svensson, *ASP Conf. Ser.*, 161, 295
- Bianchi, S., Guainazzi, M., Matt, G., Fonseca Bonilla, N., & Ponti, G. 2009, *A&A*, 495, 421
- Brenneman, L. W., Madejski, G., Fuerst, F., et al. 2014, *ApJ*, 788, 61
- Buisson, D. J. K., Parker, M. L., Kara, E., et al. 2018, *MNRAS*, 480, 3689
- Cash, W. 1979, *ApJ*, 228, 939
- Chartas, G., Kochanek, C. S., Dai, X., Poindexter, S., & Garmire, G. 2009, *ApJ*, 693, 174
- Coppi, P. S., & Zdziarski, A. A. 1992, *ApJ*, 398, L37
- Dadina, M. 2007, *A&A*, 461, 1209
- De Marco, B., Ponti, G., Cappi, M., et al. 2013, *MNRAS*, 431, 2441
- De Rosa, A., Fabian, A. C., & Piro, L. 2002, *MNRAS*, 334, L21
- Fabian, A. C., Lohfink, A., Kara, E., et al. 2015, *MNRAS*, 451, 4375
- Fabian, A. C., Lohfink, A., Belmont, R., Malzac, J., & Coppi, P. 2017, *MNRAS*, 467, 2566
- Ghisellini, G. 2013, in *Radiative Processes in High Energy Astrophysics* (Berlin: Springer Verlag), *Lect. Notes Phys.*, 873
- Haardt, F., & Maraschi, L. 1991, *ApJ*, 380, L51
- Haardt, F., & Maraschi, L. 1993, *ApJ*, 413, 507
- Haardt, F., Maraschi, L., & Ghisellini, G. 1994, *ApJ*, 432, L95
- Harrison, F. A., Craig, W. W., Christensen, F. E., et al. 2013, *ApJ*, 770, 103
- Kara, E., Alston, W., & Fabian, A. 2016, *Astron. Nachr.*, 337, 473
- Kara, E., García, J. A., Lohfink, A., et al. 2017, *MNRAS*, 468, 3489
- Lanzuisi, G., Perna, M., Comastri, A., et al. 2016, *A&A*, 590, A77
- Lanzuisi, G., Gilli, R., Cappi, M., et al. 2019, *ApJ*, 875, L20
- Lohfink, A. M., Ogle, P., Tombesi, F., et al. 2015, *ApJ*, 814, 24
- Lohfink, A. M., Reynolds, C. S., Pinto, C., et al. 2016, *ApJ*, 821, 11
- Malizia, A., Molina, M., Bassani, L., et al. 2014, *ApJ*, 782, L25
- Marinucci, A., Matt, G., Kara, E., et al. 2014a, *MNRAS*, 440, 2347
- Marinucci, A., Matt, G., Miniutti, G., et al. 2014b, *ApJ*, 787, 83
- Marinucci, A., Matt, G., Bianchi, S., et al. 2015, *MNRAS*, 447, 160
- Marinucci, A., Bianchi, S., Braitto, V., et al. 2018, *MNRAS*, 478, 5638
- Marinucci, A., Porquet, D., Tamborra, F., et al. 2019, *A&A*, 623, A12
- Matt, G., Baloković, M., Marinucci, A., et al. 2015, *MNRAS*, 447, 3029
- Middei, R., Bianchi, S., Cappi, M., et al. 2018a, *A&A*, 615, A163
- Middei, R., Vagnetti, F., Tombesi, F., et al. 2018b, *A&A*, 618, A167
- Molina, M., Bassani, L., Malizia, A., et al. 2009, *MNRAS*, 399, 1293
- Molina, M., Bassani, L., Malizia, A., et al. 2013, *MNRAS*, 433, 1687
- Morgan, C. W., Hainline, L. J., Chen, B., et al. 2012, *ApJ*, 756, 52
- Nicastro, F., Piro, L., De Rosa, A., et al. 2000, *ApJ*, 536, 718
- Parker, M. L., Wilkins, D. R., Fabian, A. C., et al. 2014, *MNRAS*, 443, 1723
- Petrola, G. C., Matt, G., Cappi, M., et al. 2002, *A&A*, 389, 802
- Petrucci, P. O., Haardt, F., Maraschi, L., et al. 2000, *ApJ*, 540, 131
- Petrucci, P. O., Haardt, F., Maraschi, L., et al. 2001, *ApJ*, 556, 716
- Porquet, D., Reeves, J. N., Matt, G., et al. 2018, *A&A*, 609, A42
- Poutanen, J., & Svensson, R. 1996, *ApJ*, 470, 249
- Rani, P., Stalin, C. S., & Goswami, K. D. 2019, *MNRAS*, 484, 5113
- Ricci, C., Ho, L. C., Fabian, A. C., et al. 2018, *MNRAS*, 480, 1819
- Risaliti, G., Nardini, E., Salvati, M., et al. 2011, *MNRAS*, 410, 1027
- Serafinelli, R., Vagnetti, F., & Middei, R. 2017, *A&A*, 600, A101
- Sobolewska, M. A., & Papadakis, I. E. 2009, *MNRAS*, 399, 1597
- Tamborra, F., Matt, G., Bianchi, S., & Dovčiak, M. 2018, *A&A*, 619, A105
- Titarchuk, L. 1994, *ApJ*, 434, 570
- Tortosa, A., Marinucci, A., Matt, G., et al. 2017, *MNRAS*, 466, 4193
- Tortosa, A., Bianchi, S., Marinucci, A., Matt, G., & Petrucci, P. O. 2018a, *A&A*, 614, A37
- Tortosa, A., Bianchi, S., Marinucci, A., et al. 2018b, *MNRAS*, 473, 3104
- Ursini, F., Boissay, R., Petrucci, P.-O., et al. 2015, *A&A*, 577, A38
- Ursini, F., Petrucci, P.-O., Matt, G., et al. 2016, *MNRAS*, 463, 382
- Uttley, P., Cackett, E. M., Fabian, A. C., Kara, E., & Wilkins, D. R. 2014, *A&ARv*, 22, 72
- Younes, G., Ptak, A., Ho, L. C., et al. 2019, *ApJ*, 870, 73
- Young, A. J., McHardy, I., Emmanoulopoulos, D., & Connolly, S. 2018, *MNRAS*, 476, 5698
- Zdziarski, A. A., Johnson, W. N., & Magdziarz, P. 1996, *MNRAS*, 283, 193